J. Fluid Mech. (1993), *vol.* 252, *pp.* 543–564

A study of argon thermal plasma flow over a solid sphere

By SEUNGHO PAIK[1], HOA D. NGUYEN[1] AND JACOB N. CHUNG[2]

[1] Idaho National Engineering Laboratory, EG & G Idaho, Inc., P.O. Box 1625,
MS 2404 Idaho Falls, ID 83415, USA

[2] Department of Mechanical and Materials Engineering, Washington State University, Pullman,
WA 99164-2920, USA

(Received 28 February 1992 and in revised form 21 January 1993)

The phenomena of momentum and heat transfer associated with an impulsively started spherical particle in a quiescent argon thermal plasma environment is considered. The changing plasma thermodynamics and transport property effects are studied using a Chebyshev–Legendre spectral method. Steady-state solutions for the case of constant sphere surface temperature are obtained and compared with previously published results. Transient solutions with particle internal heat conduction included are also presented. Results indicate that the magnitude of the drag force increases as the plasma free-stream temperature increases, while the Nusselt number decreases with increasing free-stream temperature. Effects due to different initial particle temperatures on the transient Nusselt number and drag coefficient are demonstrated.

1. Introduction

Studies of thermal plasma flow over a solid sphere have been pursued during the past few decades owing to its wide range of applications, such as those in chemical processing of fine powders or liquid droplets. Specific applications would include the decomposition and synthesis of materials, plasma spraying, plasma waste destruction, plasma spheroidizing, plasma fuming, etc. In these applications, fine powders or liquid droplets are injected into the high-temperature plasma causing the particles to reach a desired physical/chemical state.

Thermal plasmas provide extremely high heating and quenching rates for injected particulate matter due to their high temperatures, usually on the order of 10000 K. Under these extremely high temperatures, the injected particle experiences unusually steep temperature and velocity gradients near its surface. The transport correlations based on ordinary gas flow over a sphere fail to provide accurate predictions of the drag force and heat flux to the particle. Previous studies on this problem have been focused on obtaining steady-state momentum and heat transfer correlations. Pfender (1989) provides an extensive review on this subject. He concludes that the most important factors which make the plasma–particle momentum and heat transfer differ from those of ordinary gas flow over a sphere are the plasma thermodynamics and transport property changes due to the steep temperature gradient near the particle surface.

The momentum transfer from a thermal plasma to a solid particle has been analysed for the typical case of creeping flow due to the small size (usually in the range of 5–100 μm in diameter) of the particles used in thermal plasma processing (see Lewis &

Gauvin 1973). Early studies on the drag force exerted on a particle under thermal plasma conditions have concentrated on the extension of the well-known drag coefficient correlation at low Reynolds number ($Re < 100$, see White 1974),

$$C_D = \frac{12}{Re} + \frac{3}{1+Re^{\frac{1}{2}}} + 0.2, \tag{1}$$

by suggesting a correction factor that accounts for the effects of the changing properties. Various forms of the modifying factor have been proposed and can be found elsewhere (see Lewis & Gauvin 1973; Pfender 1989). Owing to the short residence time of the particle inside the hot plasma region during thermal plasma particle processing (usually on the order of milliseconds), it becomes questionable whether the steady-state drag correlation can be used for predicting the plasma–particle interactions. It is not clear that the relaxation time for a particle injected into a thermal plasma is much less than a millisecond. Under certain circumstances where the particle motion is accelerated, significant relaxation times are required for the particle to adjust to the flow field. Thus the drag coefficient calculated within this flow field would give a result which would be the sum of transient and steady-state responses (Lewis & Gauvin 1973).

The effects of changing plasma thermodynamics and transport properties on the heat transfer rates are well summarized by Chen (1988). Early efforts on modifying the well-known Ranz–Marshall formula to fit plasma–particle heat transfer are concentrated on a correction factor which is a function of density, viscosity and thermal capacities. However, the plasma properties are dependent on the type of working gas as well as the temperatures and the pressures. Thus, the predicted heat flux based on the multiplying factor methods from air plasma is higher than that from argon plasma. The calculated Nusselt numbers based on the correcting factors recommended by various researchers deviate from each other significantly. It is believed that the deviations are caused by the different plasma properties and different plasma flow conditions simulated. Even though there are many suggested steady-state Nusselt numbers, again it is unclear whether a particle injected into a thermal plasma truly experiences steady-state heat transfer. Bourdin, Fauchais & Boulos (1983) used a simple heat conduction model to calculate the particle temperature history and concluded that the injected particles usually experience the melting point temperature within less than a millisecond. Particle sizes in the range of 20–100 μm have been simulated under various plasma free-stream conditions in their calculation. Based on these results, they concluded that the relaxation time of the thermal boundary layer around the particle is negligible compared to the transient heating time.

In the presentation which follows, the case of constant sphere surface temperature is treated first, followed by the case of time-varying sphere temperature. From these solutions, results are deduced for both the drag coefficient and the Nusselt number during the transient period.

2. Mathematical formulation

Argon is selected as the working gas for the simulation because of its relatively well-known thermodynamic and transport properties. Although this study is restricted to argon plasma, the mathematical formulation used in this study is applicable to any type of working gas for the thermal plasma. The argon plasma flow is assumed to be characterized as a thermal plasma and, due to its high temperature, the local thermodynamic equilibrium hypothesis is made for the entire flow region. However, the local thermodynamic equilibrium assumption may not be valid near a cold surface, especially near the sphere surface where the surface temperature is lower than the melting temperature of the material. To further simplify the mathematical formulation, the plasma is assumed to behave as a single continuous fluid with only one representative temperature for the flow. An optically thin plasma is also assumed so that radiative energy emitted by the plasma is not absorbed by itself. Finally gravity and viscous dissipation effects on the plasma flow are neglected.

Based on the above assumptions all the governing equations, to be given in Einstein notation, are given herein. The global mass conservation equation can be written as

$$\frac{\partial \rho^*}{\partial t^*}+\frac{\partial}{\partial x_k^*}(\rho^* u_k^*)=0, \tag{2}$$

where an asterisk represents dimensional quantities and $\rho^* = \sum_i \rho_i^*$ is the total mass density of the plasma as a single fluid and ρ_i^* is the partial mass density (mass per unit volume) of species i. This study restricts the simulating plasma temperature range below 15000 K so that no more than one ionized species exists. Thus the index i represents electron, single charged ion, and atom. Without an externally applied electromagnetic field, the electrons and heavy species can be assumed to have the same velocity, thus the velocity u_k^* stands for the representative species' velocity considered in this study.

The conservation of momentum is governed by the Navier–Stokes equation written as

$$\frac{\partial u_j^*}{\partial t^*}+u_k^*\frac{\partial u_j^*}{\partial x_k^*}=-\frac{1}{\rho^*}\frac{\partial p^*}{\partial x_j^*}+\frac{1}{\rho^*}\frac{\partial}{\partial x_j^*}\left(\lambda^*\frac{\partial u_k^*}{\partial x_k^*}\right)+\frac{1}{\rho^*}\frac{\partial}{\partial x_i^*}\left[\mu^*\left(\frac{\partial u_i^*}{\partial x_j^*}+\frac{\partial u_j^*}{\partial x_i^*}\right)\right], \tag{3}$$

where indices k and i have the value of 1 or 2 for the two-dimensional formulation considered in this study. μ^* is the molecular viscosity and λ^* is the secondary viscosity coefficient. The pressure p^* is subject to Dalton's law of partial pressures, i.e. $p^* = \sum_i n_i k_B T^*$ where the summation is for electrons, ions, and atoms, and k_B is the Boltzmann constant. Note that a single temperature is used to represent the thermodynamic state of the plasma for every species in the system based on the local thermodynamic equilibrium assumption stated earlier.

The effective thermal conductivity κ^*, which accounts for the energy transfers due to ionization, recombination, thermal diffusion and equilibrium radiation, is used to describe the heat conduction. By using the effective thermal conductivity concept, the energy conservation equation can be written as

$$\rho C_p^*\left(\frac{\partial T^*}{\partial t^*}+u_k^*\frac{\partial T^*}{\partial x_k^*}\right)=\frac{\partial}{\partial x_j^*}\left(\kappa^*\frac{\partial T^*}{\partial x_j^*}\right)+Q_r^*, \tag{4}$$

where C_p^* is the total thermal capacity which includes the stagnation enthalpy as well as the translational energy. The radiative energy transfer is treated as a volumetric heat sink term since the optical depth of the radiation is assumed to be small compared to the characteristic length of the plasma. Note that $\mathrm{D}p^*/\mathrm{d}t^*$ and viscous dissipation terms are neglected because of the relatively low velocities usually encountered in thermal plasma spray and processing.

Equations (2)–(4) can now be non-dimensionalized by using the following dimensionless variables defined as:

$$\left.\begin{aligned} &t=\frac{U_\infty^* t^*}{R}, \quad u_i=\frac{u_i^*}{U_\infty^*}, \quad \rho=\frac{\rho^*}{\rho_\infty^*}, \quad \mu=\frac{\mu^*}{\mu_\infty^*}, \quad \lambda=\frac{\lambda^*}{\lambda_\infty^*}, \\ &x_i=\frac{x_i^*}{R}, \quad p=\frac{p^*}{\rho_\infty^* U_\infty^{*2}}, \quad Re_\infty=\frac{\rho_\infty^* U_\infty^* R}{\mu_\infty^*}, \quad Pr_\infty=\frac{C_{p\infty}^* \mu_\infty^*}{\kappa_\infty^*}, \\ &Z=\frac{T^*-T_\infty^*}{T_{\mathrm{I}}^*-T_\infty^*}, \quad C_p=\frac{C_p^*}{C_{p\infty}^*}, \quad \kappa=\frac{\kappa^*}{\kappa_\infty^*}, \quad q_r=\frac{Q_r^* R/(\rho_\infty^* U_\infty^* C_{p\infty}^*)}{T_{\mathrm{I}}^*-T_\infty^*} \end{aligned}\right\} \tag{5}$$

where subscript ∞ represents the free-stream condition and T_{I}^* is the initial particle temperature. Using these dimensionless variables, (2)–(4) can be recast into the non-dimensional form

$$\frac{\partial \rho}{\partial t}+\frac{\partial}{\partial x_k}(\rho u_k)=0, \tag{6}$$

$$\frac{\partial u_j}{\partial t}+u_k\frac{\partial u_j}{\partial x_k}=-\frac{1}{\rho}\frac{\partial p}{\partial x_j}+\frac{1}{Re_\infty}\left[\frac{\mu}{\rho}\frac{\partial^2 u_j}{\partial x_i \partial x_i}+\frac{1}{\rho}\frac{\partial}{\partial x_j}\left((\mu+\lambda)\frac{\partial u_k}{\partial x_k}\right)+\frac{1}{\rho}\frac{\partial \mu}{\partial x_i}\frac{\partial u_j}{\partial x_i}\right], \tag{7}$$

$$\rho C_p\left(\frac{\partial Z}{\partial t}+u_k\frac{\partial Z}{\partial x_k}\right)=\frac{1}{Re_\infty Pr_\infty}\frac{\partial}{\partial x_j}\left(\kappa\frac{\partial Z}{\partial x_j}\right)+q_r. \tag{8}$$

The above dimensionless form of the governing equations is used to calculate the flow and temperature field around the sphere.

3. Thermodynamic and transport properties

In order to solve the governing equations outlined in the previous section, it is necessary to use the plasma thermodynamic and transport properties. For argon plasma at atmospheric pressure, the properties are relatively well known over a wide range of temperatures (see Hsu 1982 and Lewis 1972).

For viscosity at $T^* < 13000$ K, the curve-fitted form of Hsu's (1982) data is used, which can be expressed as

$$\mu^* = 4.414\times 10^{-5}+1.0789\times 10^{-8}T^*+5.4642\times 10^{-12}T^{*2} -4.1681\times 10^{-16}T^{*3}\ \mathrm{kg\ m^{-1}\ s^{-1}}.$$

For the secondary viscosity coefficient, the Stokesian relation, i.e.

$$\mu^*+\tfrac{2}{3}\lambda^*=0$$

is used. Since the local thermodynamic equilibrium assumption used in this study implies a Boltzmann distribution of the thermal energies among the individual species, the Stokes' hypothesis is valid. For the density, heat capacity, thermal conductivity, and volumetric radiation loss term, the expressions used by Miller & Ayen (1969) are adopted in this study. They can be written

Density
$T^* < 16000$ K:
$\rho^* = 1.783[273/T^*-2.06\times 10^{-7}T^*+6.72\times 10^{-11}T^{*2}-5.21\times 10^{-15}T^{*3}]$ kg m^{-3};
Heat capacity
$T^* < 6000$ K: $C_p^* = 518.8$ J (kg K)$^{-1}$;
$6000 \leqslant T^* < 10000$ K: $C_p^* = 518.8+995.8(T^*\times 10^{-4})^{11}$ *J (kg K)*$^{-1}$;
$10000 \leqslant T^* < 13500$ K: $C_p^* = 518.8+995.8(T^*\times 10^{-4})$ J (kg K)$^{-1}$;
Thermal conductivity
$500 < T^* < 6000$ K:
$\kappa^* = -0.024(T^*\times 10^{-4})^2+0.262(T^*\times 10^{-4})+0.0165$ W (m K)$^{-1}$;

$6000 \leqslant T^* < 12000$ K:
$\kappa^* = 0.248(T^* \times 10^{-4})^6 + 0.372(T^* \times 10^{-4})^3 + 0.074$ W (m K)$^{-1}$;
Radiation loss
$T^* > 9500$ K: $Q_r^* = 5600(T^* - 9500) + 181(T^* - 9500)^2$ W m^{-3}.

4. Calculation method

Figure 1 illustrates the physical configuration and geometry under consideration in a two-dimensional spherical coordinates system (r, θ) with the origin taken to be at the centre of the sphere. As depicted, a rigid particle, assumed spherical in shape, of radius R and at temperature T_{I}^* is exposed to an unbounded compressible fluid at temperature T_∞^*. At the time of exposure $(t = 0)$, the motion of the sphere is started in an impulsive fashion such that the flow is instantaneously accelerated from rest to U_∞^* heading from right to left.

The spectral method adopted in this study uses Chebyshev and Legendre polynomials as basis functions for series expansions in the radial and angular directions, respectively. The radial coordinate is made finite by projecting the outer region of the solid sphere, initially infinite, into a spherical shell. Further, the normal distance between the two concentric spheres is rescaled using a new variable $\eta \in [-1, 1]$. This coordinate transformation is obtained by the use of an exponential mapping, which results in a dense distribution of collocation points near the sphere surface where the velocity gradients are expected to be large. The coordinate transformation can be written as

$$r = \exp[(1-\eta)\eta_\infty/2], \tag{9}$$

where η_∞ is a parameter large enough such that the flow at any point with radius greater than $\exp(\eta_\infty)$ would behave like the free stream. The angular coordinate is mapped into a new variable $\chi = \cos\theta$, so that we can expand the dependent variable as series of Legendre and associated Legendre polynomials, i.e.

$$\left.\begin{aligned} u_r &= \sum_{n=1}^{N_{\mathrm{L}}} U_n(t,\eta)P_n(\chi), & u_\theta &= \sum_{n=1}^{N_{\mathrm{L}}} V_n(t,\eta)P_n^1(\chi), \\ p &= \sum_{n=1}^{N_{\mathrm{L}}} A_n(t,\eta)P_n(\chi), & Z &= \sum_{n=0}^{N_{\mathrm{L}}} Z_n(t,\eta)P_n(\chi), \end{aligned}\right\} \tag{10}$$

where $P_n(\chi)$ is the Legendre polynomial of order n, $P_n^1(\chi)$ is the associated Legendre polynomial of the first kind and N_{L} is the number of Legendre polynomials.

The fractional time-stepping method originally used for incompressible flow calculation (Orszag & Kells 1980) is extended to calculate the compressible plasma flow. The first step of the time-stepping method treats the advection term in (7) by a second-order Adams–Bashforth method:

$$\hat{u}_j^{n+1} = \hat{u}_j^n - \Delta t\left(\tfrac{3}{2}u_k^n\frac{\partial u_j^n}{\partial x_k} - \tfrac{1}{2}u_k^{n-1}\frac{\partial u_j^{n-1}}{\partial x_k}\right), \tag{11}$$

where the superscript n represents the time level. This step is exactly the same as the one used for incompressible flow calculation (Orszag & Kells 1980). The second step is to impose the continuity equation by using a pseudo-velocity defined as

$$\hat{\hat{u}}_j^{n+1} = \hat{u}_j^{n+1} - \frac{1}{\rho}\frac{\partial p^{n+1}}{\partial x_j}, \tag{12}$$

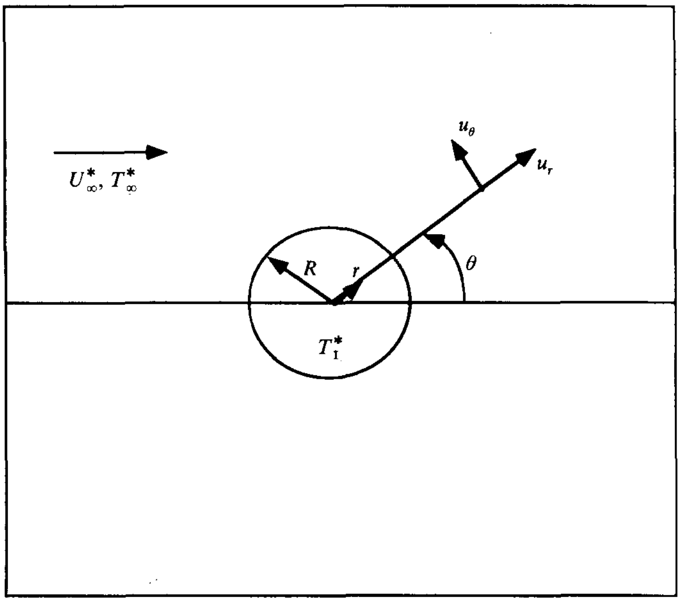

FIGURE 1. Schematic of the coordinate system.

and upon substituting this expression into (6) we then obtain

$$\frac{\partial^2 p^{n+1}}{\partial x_j \partial x_j} = \frac{\partial \rho}{\partial t} + \hat{u}_j^{n+1} \frac{\partial \rho}{\partial x_j} + \rho \frac{\partial \hat{u}_j^{n+1}}{\partial x_j}. \tag{13}$$

It should be noted that (13) contains the density variation terms which vanish in the incompressible flow formulation. Next, we express the density variation in terms of the dependent variables pressure and temperature by using the isentropic relations, i.e.

$$\frac{\partial \rho}{\partial t} = \frac{\partial \rho}{\partial Z}\frac{\partial Z}{\partial t} + \frac{\partial \rho}{\partial p}\frac{\partial p}{\partial t} = \frac{\partial \rho}{\partial Z}\frac{\partial Z}{\partial t} + M_\infty^2 \frac{\partial p}{\partial t}, \tag{14}$$

where M_∞ is the Mach number based on free-stream conditions. Similar expression can also be written for $\partial \rho / \partial x_j$. In order for the pressure-based calculation procedure to cover all the flow velocity ranges, (14) is substituted into (13). The resulting expression is

$$\frac{\partial^2 p^{n+1}}{\partial x_j \partial x_j} - M_\infty^2 \left(\frac{\partial p}{\partial t} + \hat{u}_j^{n+1} \frac{\partial p}{\partial x_j} \right) = \left(\frac{\partial \rho}{\partial Z} \right)_p \left(\frac{\partial Z}{\partial t} + \hat{u}_j^{n+1} \frac{\partial Z}{\partial x_j} \right) + \rho \frac{\partial \hat{u}_j^{n+1}}{\partial x_j}, \tag{15}$$

where the term $\partial \rho / \partial Z$ can be calculated with a known temperature field using the property information mentioned in §3. In order to maintain the compressible feature of the computer code, all the terms are retained in this study. However, in case of the argon plasma–particle interactions, the typical free-stream Mach number normally encountered is less than 0.1, thus it seems that the term involving the Mach number does not play an important role in the cases simulated throughout this study. After solving (15), the pseudo-velocity is updated by using equation (12). Finally, the third step involves the viscous terms and is advanced by the backward Euler difference, where actual velocity is calculated as

$$u_j^{n+1} = \hat{u}_j^{n+1} + \frac{\Delta t}{Re_\infty} \left[\frac{\mu}{\rho} \frac{\partial^2 u_j^{n+1}}{\partial x_i \partial x_i} + \frac{1}{3\rho} \left(\frac{\partial \mu}{\partial x_k} \frac{\partial u_k^{n+1}}{\partial x_j} + \mu \frac{\partial^2 u_k^{n+1}}{\partial x_k \partial x_j} \right) + \frac{1}{\rho} \frac{\partial \mu}{\partial x_l} \frac{\partial u_j^{n+1}}{\partial x_l} \right]. \tag{16}$$

The temperature equation is solved implicitly using the backward Euler difference as

$$\frac{Z^{n+1}-Z^{n}}{\Delta t}+u_k^{n+1}\frac{\partial Z^{n+1}}{\partial x_k}=\frac{1}{Re_\infty Pr_\infty}\frac{\partial}{\partial x_j}\left(\kappa\frac{\partial Z^{n+1}}{\partial x_j}\right)+q_r^n. \tag{17}$$

Since the dependence of the plasma thermodynamics and transport properties on the temperature is strong, (15)–(17) are solved iteratively.

Equations (16) and (17) involve the spatial derivative of viscosity and thermal conductivity, which can be written as

$$\frac{\partial \mu}{\partial x_j}=\frac{\partial \mu}{\partial Z}\frac{\partial Z}{\partial x_j},\quad \frac{\partial \kappa}{\partial x_j}=\frac{\partial \kappa}{\partial Z}\frac{\partial Z}{\partial x_j}, \tag{18}$$

where only the temperature dependence of the viscosity is taken into account. The variations of viscosity and thermal conductivities with temperature are evaluated at constant pressure.

It is well known that for Stokes flow the boundary layer is theoretically infinite in extent. Thus different values of η_∞ result in different converged solutions. Our previous study (Paik, Nguyen & Chung 1992) for ordinary gas glow over a solid sphere indicated that choice of $\eta_\infty = 3$ does not change the converged solution appreciably, thus the value of η_∞ is fixed at 3 throughout the present study. The collocation method used in this study evaluates all the spatial derivatives in physical space. The detailed representation of the derivatives in spectral form can be found in Nguyen, Paik & Chung (1991).

At this point, it is necessary to discuss the convergence of the numerical scheme described in this section. In Practice, Orszag's splitting method has been proved to converge to reasonably accurate results for the simulation of incompressible Newtonian fluid motion even though it employs a mathematically improper pressure boundary condition at the solid surface (Karniadakis, Israeli & Orszag 1991; Orszag, Israeli & Deville 1986; Temam 1991). However, since the present formulation extends the application of the scheme to compressible flow simulation we performed a convergence study. The mass and momentum residuals are used for the convergence indicator, which are defined as

for the mass residual:

$$\begin{aligned}R_{n,j}=\frac{2}{2n+1}&\left\{\frac{\partial U_{n,j}}{\partial r}+\frac{2}{r}U_{n,j}+\frac{V_{n,j}}{r}n(n+1)\right\}\\&+\frac{1}{\rho}\frac{\partial \rho}{\partial Z_{n,j}}\left\{\frac{2}{2n+1}\frac{\partial Z_{n,j}}{\partial t}+\sum_{l=0}^{N_\mathrm{L}}\sum_{m=1}^{N_\mathrm{L}}\left[\alpha_{lm}^{n}\frac{\partial Z_{l,j}}{\partial r}U_{m,j}-\frac{1}{r}\beta_{lm}^{n}Z_{l,j}U_{m,j}\right]\right]\right\},\end{aligned} \tag{19}$$

for the r-momentum residual:

$$\begin{aligned}R_{n,j}^{r-m}=&\frac{Re_\infty}{\Delta t}(\hat{\hat{U}}_{n,j}-U_{n,j})+\frac{\mathrm{d}^2U_{n,j}}{\mathrm{d}r^2}+\frac{2}{r}\frac{\mathrm{d}U_{n,j}}{\mathrm{d}r}-\frac{n(n+1)}{r^2}(U_{n,j}-V_{n,j})-\frac{2U_{n,j}}{r^2}\\&+\frac{2n+1}{2}C_\mu\sum_{m=0}^{N_\mathrm{L}}\left\{2\frac{\mathrm{d}U_{n,j}}{\mathrm{d}r}\frac{\mathrm{d}Z_{m,j}}{\mathrm{d}r}\alpha_{nn}^{m}+\frac{1}{r^2}U_{n,j}Z_{m,j}\beta_{nn}^{n}\right.\\&-\sum_{k=1}^{N_\mathrm{L}}\left(\frac{1}{r}\frac{\mathrm{d}V_{k,j}}{\mathrm{d}r}Z_{m,j}\alpha_{kn}^{m}-\frac{1}{r^2}V_{k,j}Z_{m,j}\beta_{kn}^{n}\right)\\&\left.+\sum_{\substack{k=1\\k\neq n}}^{N_\mathrm{L}}\left(2\frac{\mathrm{d}U_{k,j}}{\mathrm{d}r}\frac{dZ_{m,j}}{\mathrm{d}r}\alpha_{kn}^{m}+\frac{1}{r^2}U_{k,j}Z_{m,j}\beta_{kn}^{n}\right)\right\},\end{aligned} \tag{20}$$

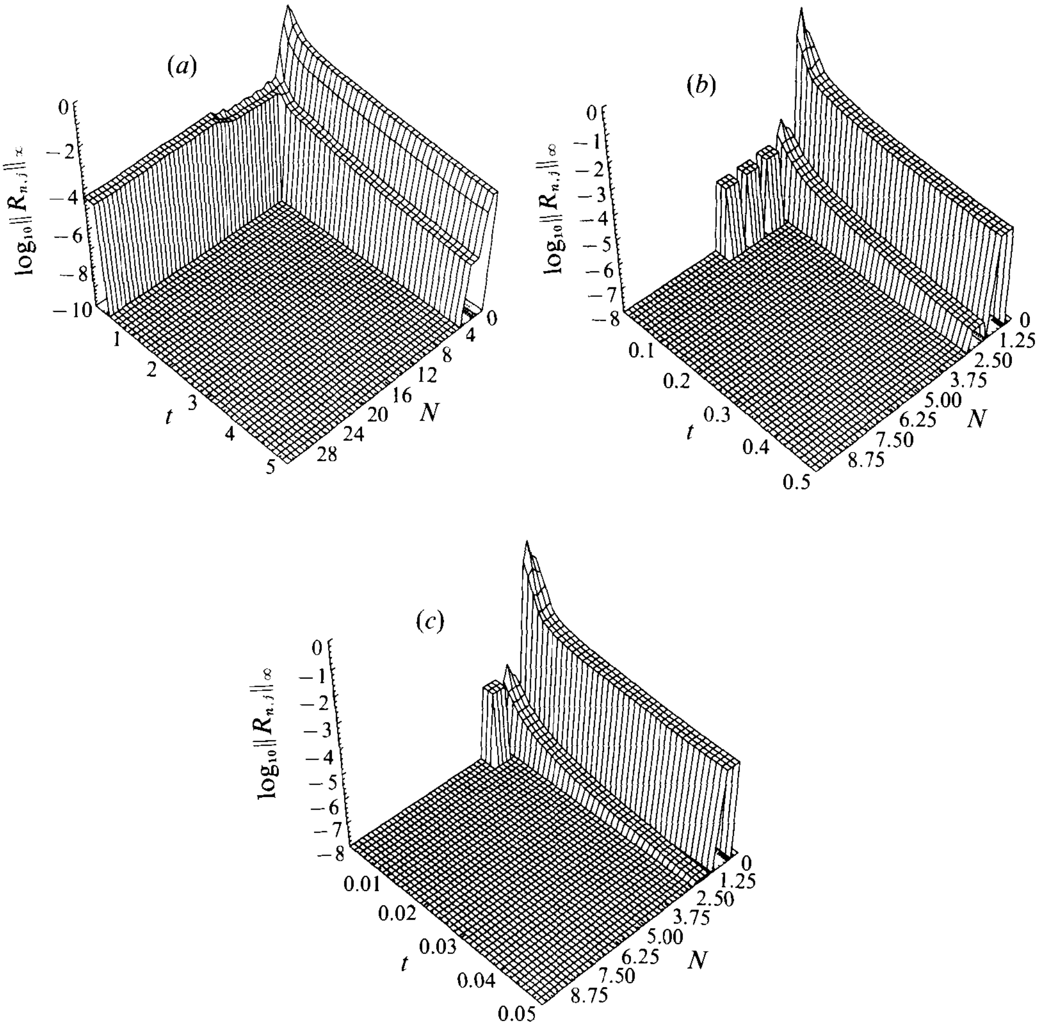

FIGURE 2. Comparison of mass residual variation with dimensionless time and number of iterations, N for (a) $\Delta t = 0.01$, (b) $\Delta t = 0.001$, (c) $\Delta t = 0.0001$.

for the θ-momentum residual:

$$\begin{aligned} R_{n,j}^{\theta-m} = {} & \frac{Re_\infty}{\Delta t}(V_{n,j}^{\text{old}} - V_{n,j}) + \frac{\mathrm{d}^2 V_{n,j}}{\mathrm{d}r^2} + \frac{2}{r}\frac{\mathrm{d}V_{n,j}}{\mathrm{d}r} - \frac{n(n+1)}{r^2}V_{n,j} - \frac{2U_{n,j}}{r^2} \\ & + \frac{2n+1}{2n(n+1)}C_\mu \sum_{m=0}^{N_\mathrm{L}} \left\{ \frac{1}{r^2} V_{n,j} Z_{m,j} \gamma_{nn}^m + \left(\frac{\mathrm{d}V_{n,j}}{\mathrm{d}r} - \frac{1}{r} V_{m,j} \right) \beta_{nn}^n \right. \\ & - \sum_{k=1}^{N_\mathrm{L}} \left(\frac{2}{r^2} U_{k,j} Z_{m,j} \lambda_{kn}^m + \frac{1}{r} U_{k,j} \frac{\mathrm{d}Z_{m,j}}{\mathrm{d}r} \beta_{kn}^n \right) \\ & \left. + \sum_{\substack{k=1 \\ k \neq n}}^{N_\mathrm{L}} \left(\frac{1}{r^2} V_{k,j} Z_{m,j} \lambda_{kn}^m + \frac{1}{r^2} \left(\frac{\mathrm{d}V_{k,j}}{\mathrm{d}r} - \frac{1}{r} V_{k,j} \right) Z_{m,j} \beta_{kn}^n \right) \right\}, \end{aligned} \tag{21}$$

where subscripts n and j represent the nth component of the Legendre polynomial at the jth collocation point, C_μ is the term containing the viscosity derivatives, and

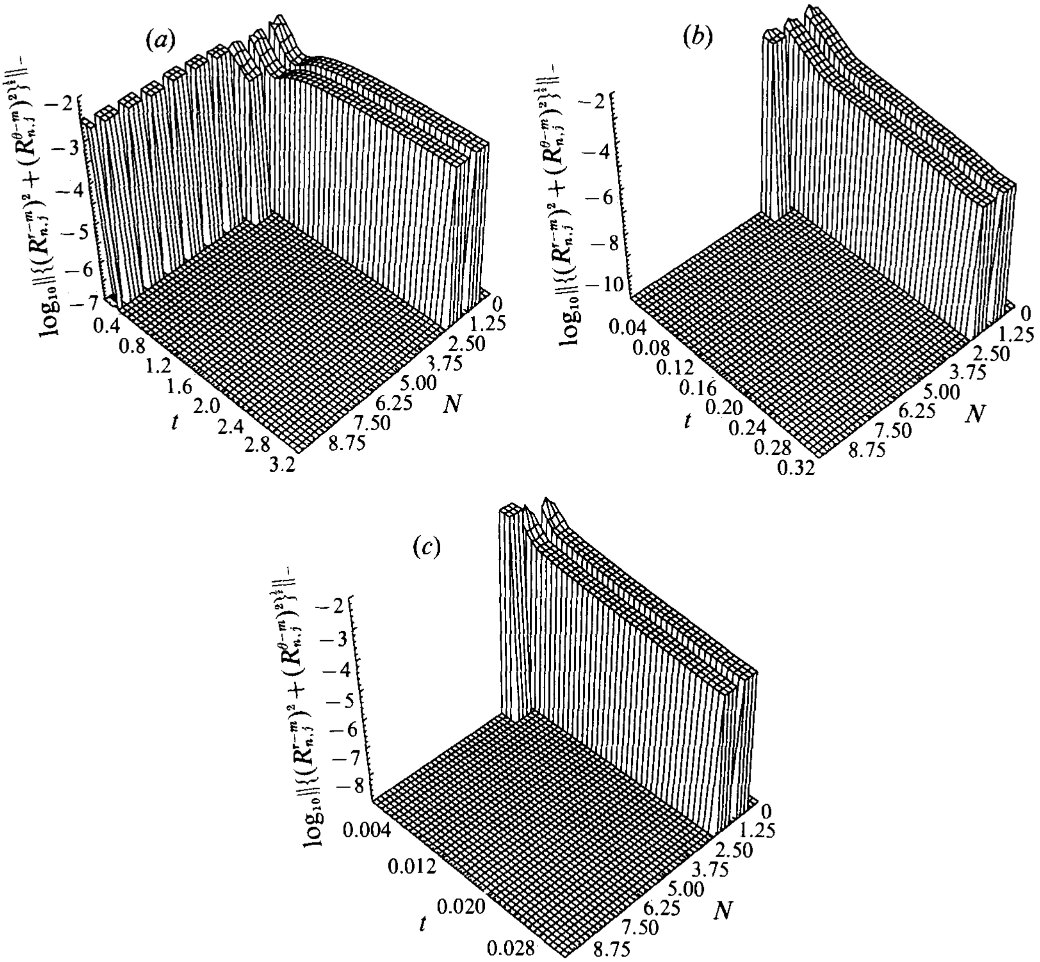

FIGURE 3. Comparison of momentum residual variation with time and N for (*a*) $\Delta t = 0.01$, (*b*) $\Delta t = 0.001$, (*c*) $\Delta t = 0.0001$.

$\alpha^n_{lm}, \beta^n_{lm}, \lambda^n_{lm}, \gamma^n_{lm}$ are constants representing the integrals of products of three associated Legendre functions. Rottenberg *et al.* (1959) presented a theory expressing these constants in terms of 3-*J* symbols, and devised algorithms to compute them numerically. Using their notation we write

$$\alpha^n_{lm} = (2n+1)\begin{pmatrix} n & l & m \\ 0 & 0 & 0 \end{pmatrix}\begin{pmatrix} n & l & m \\ 0 & 0 & 0 \end{pmatrix}, \tag{22}$$

$$\beta^n_{lm} = -(2n+1)\left[\frac{m(m+1)}{n(n+1)}\right]^{\frac{1}{2}}\begin{pmatrix} n & l & m \\ 1 & 0 & -1 \end{pmatrix}\begin{pmatrix} n & l & m \\ 0 & 0 & 0 \end{pmatrix}, \tag{23}$$

$$\lambda^n_{lm} = -(2n+1)\left[\frac{m(m+1)}{n(n+1)}\right]^{\frac{1}{2}}\begin{pmatrix} n & l & m \\ -1 & 0 & 1 \end{pmatrix}\begin{pmatrix} n & l & m \\ 0 & 0 & 0 \end{pmatrix}, \tag{24}$$

$$\gamma^n_{lm} = \lambda^n_{lm} - m(m+1)\,\beta^n_{lm}. \tag{25}$$

Figures 2 and 3 show the time history of $\log_{10}\|R_{n,j}\|_\infty$ and $\log_{10}\|\{(R^{r-m}_{n,j})^2+(R^{\theta-m}_{n,j})^2\}^{\frac{1}{2}}\|_\infty$ for a typical simulation with $Re_\infty = 20$, $T^*_\infty = 10000$ K, and $T^*_w = 3000$ K, where T^*_w is the surface temperature of the particle. The present numerical scheme is subjected to the Courant time limit because of its explicit treatment of the nonlinear terms in the Navier–Stokes equations. The typical Courant time limit is on the order of 10^{-8} s for argon plasma with $Re_{\infty} = 20$, $T^*_{\infty} = 10000$ K. For a non-dimensional time increment $\Delta t = 0.01$ (which is equivalent to $\Delta t^* = 2 \times 10^{-9}$ s, figures 2*a* and 3*a*), at the first time step, it takes more than 30 iterations for the maximum mass residual to reach 10^{-5}, which is not quite satisfactory. Furthermore, the momentum residual does not decay monotonically at that time-step size. However it takes less than four iterations for the maximum mass residual to reach 10^{-7} at the first time step for $\Delta t = 10^{-3}$ and 10^{-4} (figures 2*b* and 2*c*, respectively) and the momentum residual decays monotonically. Also, the mass and momentum residuals show exponential decay as the number of iterations increases for every time step. Thus it can be said that the present numerical scheme is convergent within the Courant time limit.

5. Results for constant surface temperature

In the ideal case of a sphere having high heat capacity and thermal conductivity, the sphere can be characterized by a constant surface temperature. Many previous works are based on the assumption of constant sphere surface temperature.

The drag coefficient can be obtained from the computed pressure and velocity fields. The drag force exerted on the sphere surface can be decomposed into two components: the form drag and the viscous drag. These two components are calculated from the expressions

$$F^*_{D_\mathrm{f}} = \int_{\phi=0}^{2\pi} \int_{\theta=0}^{\pi} (-p^* \cos\theta)\, R^2 \sin\theta \, \mathrm{d}\theta \, \mathrm{d}\phi, \tag{26a}$$

$$F^*_{D_\mathrm{v}} = \int_{\phi=0}^{2\pi} \int_{\theta=0}^{\pi} (-\tau^*_{r\theta} \sin\theta + \tau^*_{rr} \cos\theta)\, R^2 \sin\theta \, \mathrm{d}\theta \, \mathrm{d}\phi, \tag{26b}$$

where $F^*_{D_\mathrm{f}}$ and $F^*_{D_\mathrm{v}}$ represent the form and viscous components, and where $\tau^*_{r\theta}$ and τ^*_{rr} are tangential and normal stress components respectively. The spectral representations of (26*a*, *b*) become

$$F^*_{D_\mathrm{f}} = -\tfrac{4}{3}\pi A_{10} (\rho^*_{\infty} U^{*2}_{\infty} R^2), \tag{27a}$$

$$F^*_{D_\mathrm{v}} = \tfrac{8}{3}\pi \mu^*_{\infty} \rho^*_{\infty} U^{*2}_{\infty} R^2 \left[V_{10} + U_{10} + \frac{2}{\eta_{\infty}} \sum_{k=1}^{N_\mathrm{L}} G^{(1)}_{1k} V_{1k} \right] \Big/ Re_{\infty}, \tag{27b}$$

where $G^{(1)}_{1k}$ is a $N_\mathrm{T}+1$ by $N_\mathrm{T}+1$ Chebyshev derivative matrix of order 1. The drag coefficient C_D is defined as

$$C_D = \frac{F_D}{\frac{1}{2}\pi \rho^*_{\infty} U^{*2}_{\infty} R^2}, \tag{28}$$

where $F_D = F_{D_\mathrm{f}} + F_{D_\mathrm{v}}$.

At this point, we study the convergence of the drag coefficients. Table 1 shows the results of our convergence study on the drag coefficient as the number of Legendre functions N_L and the number of collocation points N_T vary. We conclude that the drag coefficient is less sensitive to the number of Legendre functions than the number of collocation points. Throughout this study we use $N_\mathrm{L} = 15$ and $N_\mathrm{T} = 45$ for $Re_{\infty} \leqslant 20$, since the converged drag coefficients yield values to the order of 10^{-2} accuracy, which is within the uncertainties of plasma thermodynamic and transport properties.

Based on a finite difference study, Lee, Hsu & Pfender (1981) suggested a simple factor to account for the effects of the changing argon thermal plasma properties on the drag coefficient calculation:

$$C_D = C_{D_\mathrm{f}} (\rho^*_{\infty} \mu^*_{\infty} / \rho^*_\mathrm{w} \upsilon^*_\mathrm{w})^{-0.45}, \tag{29}$$

Re_∞	C_D $N_L = 10, N_T = 30$	 $N_L = 15, N_T = 30$	 $N_L = 15, N_T = 45$	 $N_L = 15, N_T = 60$
1	14.335	14.329	14.314	14.310
10	2.561	2.558	2.549	2.547
20	1.987	1.983	1.971	1.970

TABLE 1. Variation of C_D with N_L and N_T ($T^*_\infty = 12000$ K and $T^*_w = 3000$ K)

Case	Re^+_∞ 0.1	 1.0	 10.0	 20.0
1(*a*)	167.03	18.68	2.89	1.84
(*b*)	146.20	15.32	2.52	0.76
(*c*)	178.37	19.34	2.74	1.68
(*d*)	144.78	14.31	2.59	1.97
2(*a*)	141.06	15.78	2.44	1.55
(*b*)	N/A	N/A	N/A	N/A
(*c*)	209.65	22.49	3.08	1.86
(*d*)	123.48	13.93	2.36	1.78
3(*a*)	204.84	22.91	3.56	2.25
(*b*)	N/A	N/A	N/A	N/A
(*c*)	220.00	23.53	3.19	1.92
(*d*)	188.82	18.78	3.65	1.82
4(*a*)	173.00	19.35	3.00	1.90
(*b*)	N/A	N/A	N/A	N/A
(*c*)	272.55	28.80	3.75	2.21
(*d*)	161.93	16.08	2.51	2.42
5	122.10	13.72	2.212	1.365

TABLE 2. Comparison of drag coefficients for various Reynolds numbers based on the sphere diameter. Case 1, $T^*_\infty = 12000$ K and $T^*_w = 3000$ K; Case 2, $T^*_\infty = 10000$ K and $T^*_w = 3000$ K; Case 3, $T^*_\infty = 12000$ K and $T^*_w = 1000$ K; Case 4, $T^*_\infty = 10000$ K and $T^*_w = 1000$ K; Case 5, the isothermal and incompressible solution (Dennis & Walker 1971). (*a*) Calculation based on Lee *et al.* (1981), equation (29); (*b*) Sayegh & Gauvin (1979); (*c*) Lewis & Gauvin (1973), equation (30); (*d*) present study.

where C_{D_f} is the isothermal drag coefficient. The multiplying factor $(\rho^*_\infty \mu^*_\infty / \rho^*_w \mu^*_w)^{-0.45}$, where subscript w denotes properties of the sphere, is always greater than one for hot argon plasma flow over a cold solid sphere. Thus from (29) the predicted drag coefficient under the argon thermal plasma environment is higher than that of the isothermal case. With an assumption of Stokesian motion of the plasma, Lewis & Gauvin (1973) obtained a different form of correction factor through a finite volume approach, which can be written as

$$C_D = C_{D_{av}}(\nu^*_{av}/\nu^*_\infty)^{0.15}, \tag{30}$$

where ν^* is the kinematic viscosity and subscript av represents the properties evaluated at the arithmetic mean temperature between the free stream and the sphere surface.

Table 2 compares the drag coefficients calculated using (29), (30), to those of Sayegh & Gauvin (1979) and the present study. We use Sayegh & Gauvin's data because of their popularity among thermal plasma chemists. Isothermal drag coefficients are also compared. For Cases 1, the present results compare favourably with the numerical simulation results by Sayegh & Gauvin (1979) at low Reynolds numbers ($Re_\infty < 10$). At $Re_\infty = 20$ the drag coefficient predicted in Cases (*b*) is underestimated by more than 100%. The high Reynolds number solution ($Re_\infty > 50$) of Sayegh & Gauvin shows a negative drag coefficient, which is not physically realistic. Thus, we believe that for convection-dominated flow, their results are not reliable. The magnitudes of drag coefficients predicted from various suggested correlations deviate from each other by more than 60%. Among the suggested correlations within the plasma conditions studied in this paper, the correlation suggested by Lee *et al.* (1981) seems to agree best with the present result (within 23% at most). The difference is believed to be due to two factors. First, it is necessary to use dense grids near the solid boundary to resolve the steep temperature gradient. The grid interval near the surface used in this study is 0.09 μm which is much less than 1.5 μm they used. Important physical lengthscales (such as Debye length or mean free path length) in argon plasma are on the order of microns which we resolve with our grid. Secondly, the upwind scheme they used is highly diffusive especially for the simulation of the flow over sphere because the flow approaches the grid lines at large angles. In general, under the thermal plasma environment, the drag force exerted on the sphere is larger than that of isothermal gas flow (compare with Case 5) due to a thin relatively cold boundary layer near the sphere surface. This effect will be discussed further in the following section.

In a thermal plasma, the Nusselt number is defined as

$$Nu = \frac{2Rq^*}{S^*_\infty - S^*_w}, \tag{31}$$

where q is the heat flux to the surface and S is the heat conductivity potential defined as

$$S^*(T^*) = \int_{T^*_r}^{T^*} \kappa^* \, \mathrm{d}T^*.$$

For pure heat conduction, (31) ensures a limiting Nusselt number of 2 while other Nusselt number definitions fail (see Chen 1988). Based on this Nusselt number definition, Vardelle, Vardelle & Fauchais (1982) suggested through extensive numerical study an empirical correlation relating the Nusselt number with the Reynolds number evaluated with average plasma properties between the free stream and the surface temperatures as

$$Nu = 2 + 0.514 Re^{\frac{1}{2}}_{\infty \mathrm{av}}. \tag{32}$$

Chen (1986) suggested another form of Nusselt number expression by using the same numerical approach as Lee *et al.* (1982), which can be written as

$$Nu = 2\left[1 + 0.63 Re_\infty Pr^{0.8}_\infty \left(\frac{Pr_w}{Pr_\infty}\right)^{0.42} \left(\frac{\rho^*_\infty \mu^*_\infty}{\rho^*_w \mu^*_w}\right)^{0.52} C^2\right]^{\frac{1}{2}}, \tag{33}$$

where
$$C = [1 - (h^*_w/h^*_\infty)^{1.14}]/[1 - (h^*_w/h^*_\infty)^2]$$

and h^* is the enthalpy.

Table 3 shows the steady-state Nusselt number for different plasma free-stream temperatures under atmospheric pressure. The results are compared with the suggested correlations available in the literature. The effect of Prandtl number on the Nusselt number is omitted in (33) by the assumption of $Pr = 1$, thus the predicted Nusselt number deviation using (33) at low Reynolds number is expected to be small. This is due to the Prandtl number usually encountered in argon atmospheric thermal plasmas being on the order of 0.67 at temperatures higher than 10000 K. The Nusselt numbers

	Re_∞^+			
Case	0.1	1.0	10.0	20.0
1(*a*)	2.131	2.410	3.297	3.835
(*b*)	2.032	2.282	4.011	5.308
(*c*)	2.041	2.298	4.646	5.573
2(*a*)	2.124	2.372	3.178	3.666
(*b*)	2.032	2.229	4.109	5.457
(*c*)	2.045	2.259	3.523	4.770
3(*a*)	2.113	2.362	3.145	3.619
(*b*)	2.034	2.244	3.793	4.978
(*c*)	2.106	2.264	3.442	5.319
4(*a*)	2.105	2.318	3.123	3.426
(*b*)	2.033	2.276	3.698	5.261
(*c*)	2.054	2.363	3.572	4.521
5	2.037	2.260	3.358	4.065

TABLE 3. Comparison of Nusselt numbers for various Reynolds numbers based on the sphere diameter. Case 1, $T_\infty^* = 12000$ K and $T_w^* = 3000$ K; Case 2, $T_\infty^* = 10000$ K and $T_w^* = 3000$ K; Case 3, $T_\infty^* = 12000$ K and $T_w^* = 1000$ K; Case 4, $T_\infty^* = 10000$ K and $T_w^* = 1000$ K; Case 5, constant-fluid-property calculation with $Pr_\infty = 0.73$ (Dennis *et al.* 1973). (*a*) Calculation based on Vardelle *et al.* (1982), equation (32); (*b*) calculation based on Chen (1988), equation (33); (*c*) present study.

	Re_∞^+			
Case	0.1	1.0	10.0	20.0
1	0.132	0.234	2.001	2.983
2	0.114	0.192	1.732	2.541
3	0.141	0.262	2.585	3.248
4	0.108	0.153	1.847	2.032

TABLE 4. Time taken to reach steady state (μs) for various Reynolds numbers based on the space diameter. Cases 1–4 are defined in tables 2 and 3

at low Reynolds number ($Re < 1$) given by Vardelle *et al.* (1982) are higher than both those of Chen (1988) and the present study since the Prandtl number is implicitly assumed to be unity in their correlation, implying higher heat conductivity than the actual plasma case. In general, the present results agree with the correlation of Chen (1988) to within 15% maximum deviation. The calculated Nusselt numbers under thermal plasma conditions are higher than that of the constant-property calculations (see Case 5) due to the steep temperature gradient developed near the sphere surface.

Table 4 shows the elapsed time to reach steady state for the simulated cases. The estimation of the thermal relaxation time required to reach the steady state for fluid properties changing with temperature, as suggested by Konopliv & Sparrow (1972), is written as

$$t^* \approx \left[3\left(\frac{U_\infty^{*2}\kappa^*}{\rho^* C_p^* D_p^4}\right)^{\frac{1}{3}}\right]^{-1}. \tag{34}$$

Using this expression, the times required to reach state state for the simulated case with free-stream temperatures 12000 and 10000 K become 0.0865 and 0.03623 μs respectively. In deriving (34), Stokesian flow with quasi-steady state is assumed.

Present results show that for the low Reynolds number case ($Re_\infty = 0.1$) the time required to reach steady state is about 2 to 3 times greater than that predicted by (34). This is believed to be because the momentum boundary layer develops more slowly than the thermal boundary layer for the argon thermal plasma. As Reynolds number increases, the time necessary for the flow to reach steady state increases owing to the augmented convection effect. It is interesting to note that for the low surface temperature case, it takes longer for the flow to reach the steady state since steeper temperature and fluid property gradients near the sphere surface hinder the flow in adjusting to the environment.

Based on the present study, the time required for the particle to reach steady state is much shorter than the order of 1 ms usually encountered in thermal plasma sprays. Thus it is believed that steady-state correlations can be used for the calculation of transient particle trajectories and heating histories inside the plasma.

6. Results including internal heat conduction

In this section we consider internal heat conduction inside the particle and its overall effects on the energy and momentum transfer rate.

The governing equation for the sphere internal heat conduction can be written in dimensionless form as

$$\tilde{\rho}\tilde{C}_p \frac{\partial \tilde{Z}}{\partial t} = \frac{1}{Re_\infty Pr_\infty} \frac{\partial}{\partial x_j}\left(\tilde{\kappa} \frac{\partial \tilde{Z}}{\partial x_j}\right), \tag{35}$$

where variables with a tilde represent the interior of the sphere. The inner region of the solid sphere is also transformed into the new variable $\xi \in [-1, 1]$ which can be expressed as

$$\xi = 2r - 1, \quad r < 1. \tag{36}$$

The internal dimensionless temperature is expanded as series of Legendre polynomials:

$$\tilde{Z}(t, \xi, \mu) = \sum_{n=0}^{N_L} \tilde{Z}_n(t, \xi)\, P_n(\mu). \tag{37}$$

The heat flux and temperature continuity boundary conditions can be expressed as

$$-\tilde{\kappa}\frac{\partial \tilde{Z}(t, 1, \theta)}{\partial r} + \tilde{q}_r = -\kappa \frac{\partial Z(t, 1, \theta)}{\partial r}, \quad \tilde{Z}(t, 1, \theta) = Z(t, 1, \theta), \tag{38}$$

where κ and $\tilde{\kappa}$ are thermal conductivities of the fluid and the sphere respectively. $\tilde{q}_r$ is the dimensionless radiative heat flux at the particle surface which can be written as

$$\tilde{q}_r = \frac{\epsilon\sigma(T_\infty^{*4} - T_w^{*4})\, R}{\rho_\infty^* U_\infty^* C_{p\infty}^* (T_I^* - T_\infty^*)}, \tag{39}$$

where σ is the Stefan–Boltzmann constant and ϵ is the surface emissivity.

The internal temperature equation is solved simultaneously with the plasma energy equation where a backward Euler difference is used,

$$\tilde{\rho}\tilde{C}_p \frac{\tilde{Z}^{n+1} - \tilde{Z}^n}{\Delta t} = \frac{1}{Re_\infty Pr_\infty}\frac{\partial}{\partial x_j}\left(\tilde{\kappa}\frac{\partial \tilde{Z}^{n+1}}{\partial x_j}\right). \tag{40}$$

The influence matrix technique (Paik *et al.* 1992) is used to decompose the temperature into a linear combination of a set of auxiliary functions:

$$\begin{pmatrix} Z_n \\ \tilde{Z}_n \end{pmatrix} = \begin{pmatrix} \zeta_0 \\ \tilde{\zeta}_0 \end{pmatrix} + \beta_1 \begin{pmatrix} \zeta_1 \\ 0 \end{pmatrix} + \beta_2 \begin{pmatrix} 0 \\ \tilde{\zeta}_1 \end{pmatrix}, \tag{41}$$

Material	Density (kg m^{-3})	Melting point (K)	Specific heat (J kg^{-1} K^{-1})	Thermal conductivity (W m-1 K^{-1})
Al	2707	—	896	204
Al_2O_3	4000	2326	1242	6.3
Cu	8930	1356	425	398
1 % C-Steel	7801	—	473	33

TABLE 5. Materials studied and their corresponding physical and thermodynamic properties

T^*_∞ (K)	Re^+_∞	Experiment (Chen *et al.* 1991)	Present study
9994	20.43	1.76	1.79
10228	22.46	1.61	1.67
10472	25.13	1.60	1.56
10792	28.15	1.42	1.45
10830	30.69	1.36	1.40

TABLE 6. Comparison of calculated drag coefficients with experimental data for various Reynolds numbers based on particle diameter

where β_1 and β_2 are the unknown coefficients which can be determined from the interfacial boundary conditions: temperature and heat flux continuity. In the transformed coordinates, (38) yields a linear system, written in matrix notation as

$$\begin{pmatrix} -\dfrac{1}{\eta_\infty}\zeta_1'|_{\eta=1} & -\varPhi_\kappa \hat{\zeta}_1'|_{\xi=1} \\ \zeta_1|_{\eta=1} & -\hat{\zeta}_1|_{\xi=1} \end{pmatrix} \begin{pmatrix} \beta_1 \\ \beta_2 \end{pmatrix} = \begin{pmatrix} \dfrac{1}{\eta_\infty}\zeta_0'|_{\eta=1} & +\varPhi_\kappa \hat{\zeta}_0'|_{\xi=1} + \dfrac{\tilde{q}_r}{\kappa} \\ \cdot\, \hat{\zeta}_0|_{\xi=1} & -\zeta_0|_{\eta=1} \end{pmatrix}, \tag{42}$$

in which the prime indicates the derivative with respect to the corresponding variable.

Owing to the difficulty of experimentally determining the drag coefficient and Nusselt number for particle–plasma flow, very little experimental data is available for the drag coefficient. Recently, Asamaliev *et al.* (1991) reported a drag force acting on an aluminium (Al) particle with diameter 300 μm in an argon plasma flow with $T^*_\infty = 10000$ K and $U^*_\infty = 100$ m/s. Based on their experimental conditions, $Re_\infty = 2.45$ is used to simulate the experiment. The properties for an Al particle are listed in table 5. The calculated drag force is 0.00417 N which is less than the reported value of 0.0044 N. However, considering the experimental uncertainties, the calculated drag force agrees reasonably well with the experimental data. Chen, Qui & Yang (1991) measured the drag coefficients of argon plasma on a 2.2 mm steel sphere. In order to obtain the drag force without the undesired effect of the supporting wire, they used a symmetrically welded L-shaped supporting wire. The type of steel they used in their experiments is not specified, thus we choose to use 1 % c-steel properties for our simulation. Table 6 compares the calculated drag coefficients with the experimental data. The calculated drag coefficients include the sphere internal heat conduction since it is believed that this case is close to the experimental conditions. $N_T = 60$ and $N_L = 20$ are used for the calculations and the values are obtained after 70 dimensionless time units are elapsed. The calculated drag coefficients agree with their experimental data reasonably well considered experimental uncertainties.

A calculation has been performed with Al_2O_3 and Cu particles whose properties are listed in table 5. Figure 4 shows temperature contours over an Al_2O_3 spherical particle

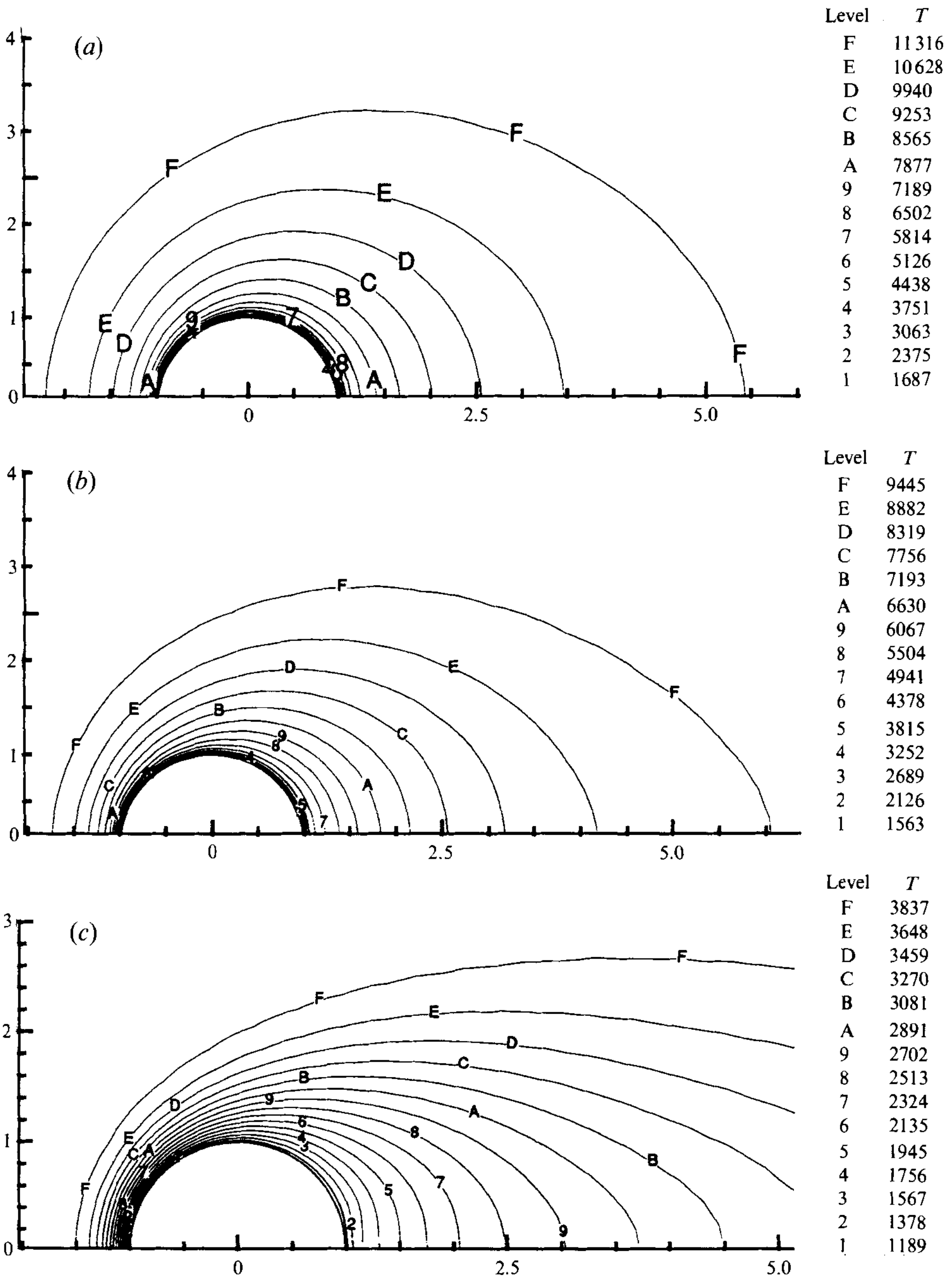

FIGURE 4. Isotherms around an Al_2O_3 particle after $t = 120$ units at $T_w^* = 1000$ K. (*a*) $T_\infty^* = 12000$ K, $t^* = 0.0071$ µs; (*b*) $T_\infty^* = 10000$ K, $t^* = 0.0082$ µs; (*c*) $T_\infty^* = 4000$ K, $t^* = 0.0383$ µs.

with radius 20 µm after 120 units of the dimensionless time. Different plasma free-stream temperatures with an initial particle temperature of 1000 K are used. For a plasma free-stream temperature of 12000 K, conduction is still the dominant heat transfer mechanism. Convection takes longer to establish than for lower free-stream temperatures due to the high thermal conductivity of the plasma at high temperature. Accordingly, convection effects are predominant for the same dimensionless timescale plots at lower free-stream temperatures (figure 4*b*, *c*). A larger temperature gradient

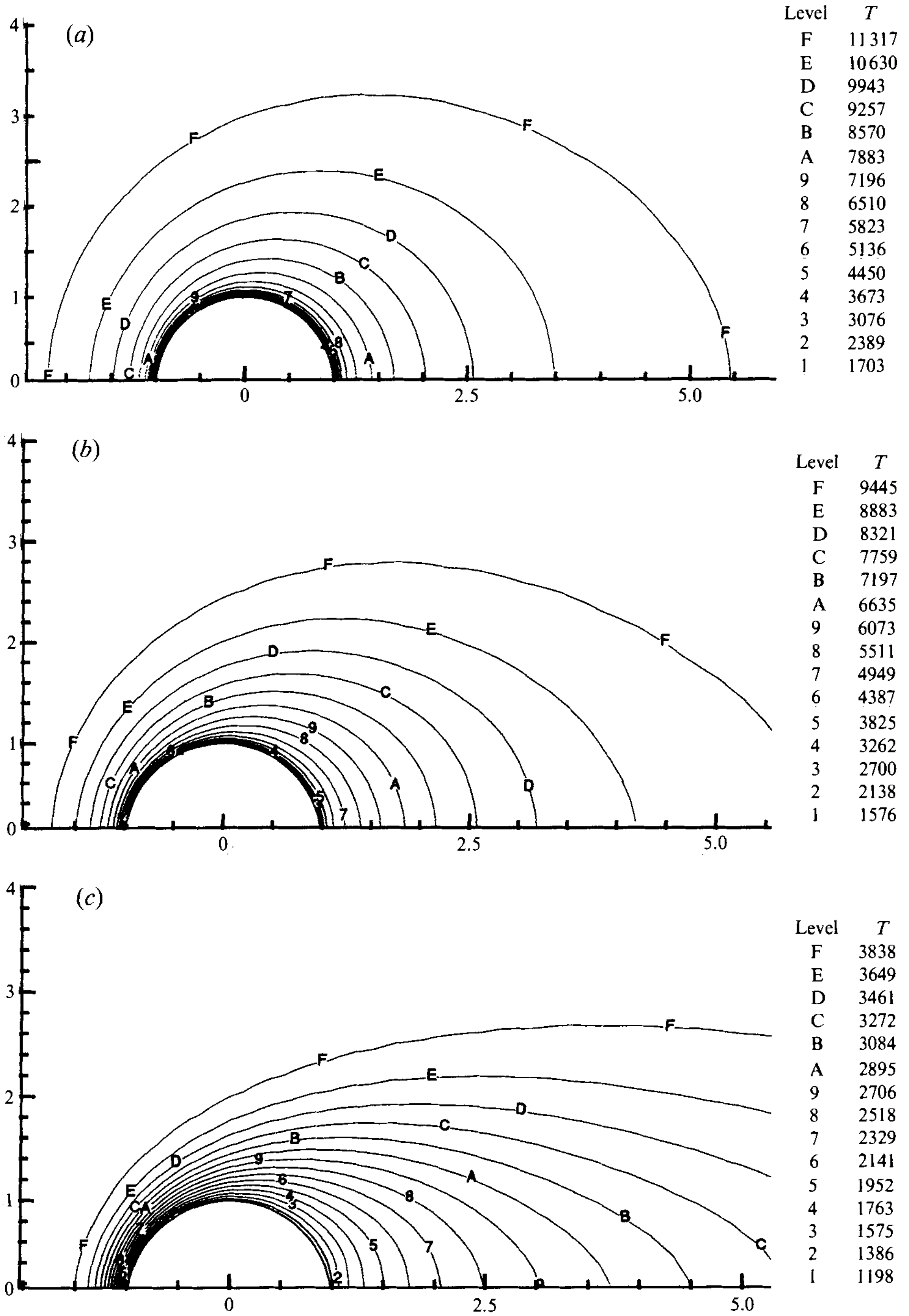

FIGURE 5. Isotherms around a Cu particle after $t = 120$ units at $T_w^* = 1000$ K. (*a*) $T_\infty^* = 12000$ K, $t^* = 0.0071$ μs; (*b*) $T_\infty^* = 10000$ K, $t^* = 0.0082$ μs; (*c*) ($T_\infty^* = 4000$ K, $t^* = 0.0383$ μs.

near the sphere surface is found for the high free-stream temperature case, which results in a higher heat transfer rate to the sphere surface. A copper particle with radius 20 μm immersed in argon plasma is simulated and the isotherms are shown in figure 5. For plasma free-stream temperatures of 12000 and 10000 K, the particle surface

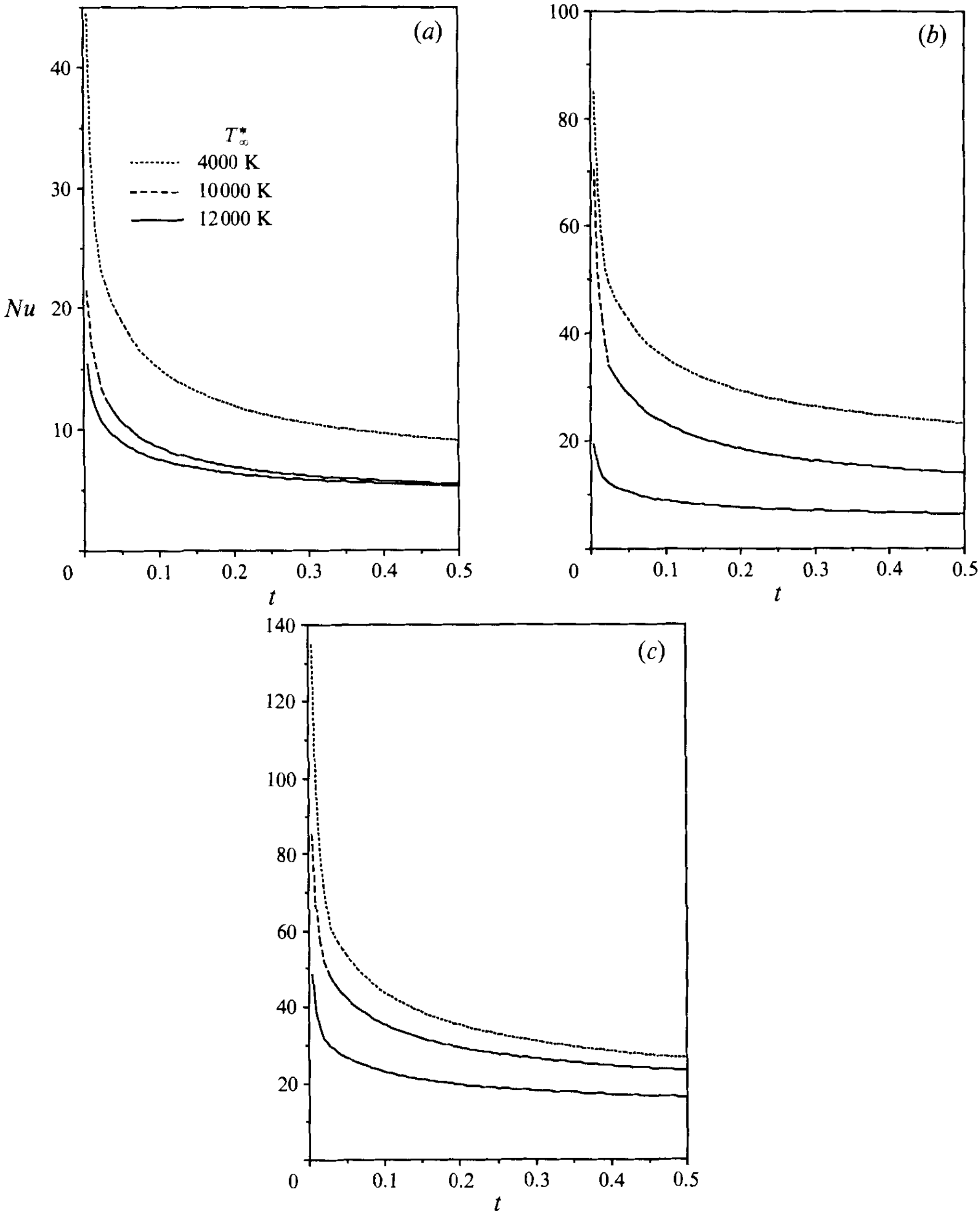

FIGURE 6. Transient Nusselt numbers for an Al_2O_3 particle for different plasma free-stream temperatures with (a) T^*_w = 1000 K, (b) = 2000 K, (c) = 3000 K.

experiences temperatures above the melting point. The actual elapsed times for the copper particle surface to reach the melting temperature are 143 and 214 dimensionless time units for the 12000 and 10000 K free-stream temperatures respectively. Because of the higher thermal conductivity and lower heat capacity of copper compared to the alumina particle, the surface temperature of the copper is higher than that of the alumina particle under the same conditions.

Figure 6 shows the calculated transient Nusselt number for the Al_2O_3 particle under different plasma free-stream and particle initial temperatures. $Re_\infty = 20$ is used with

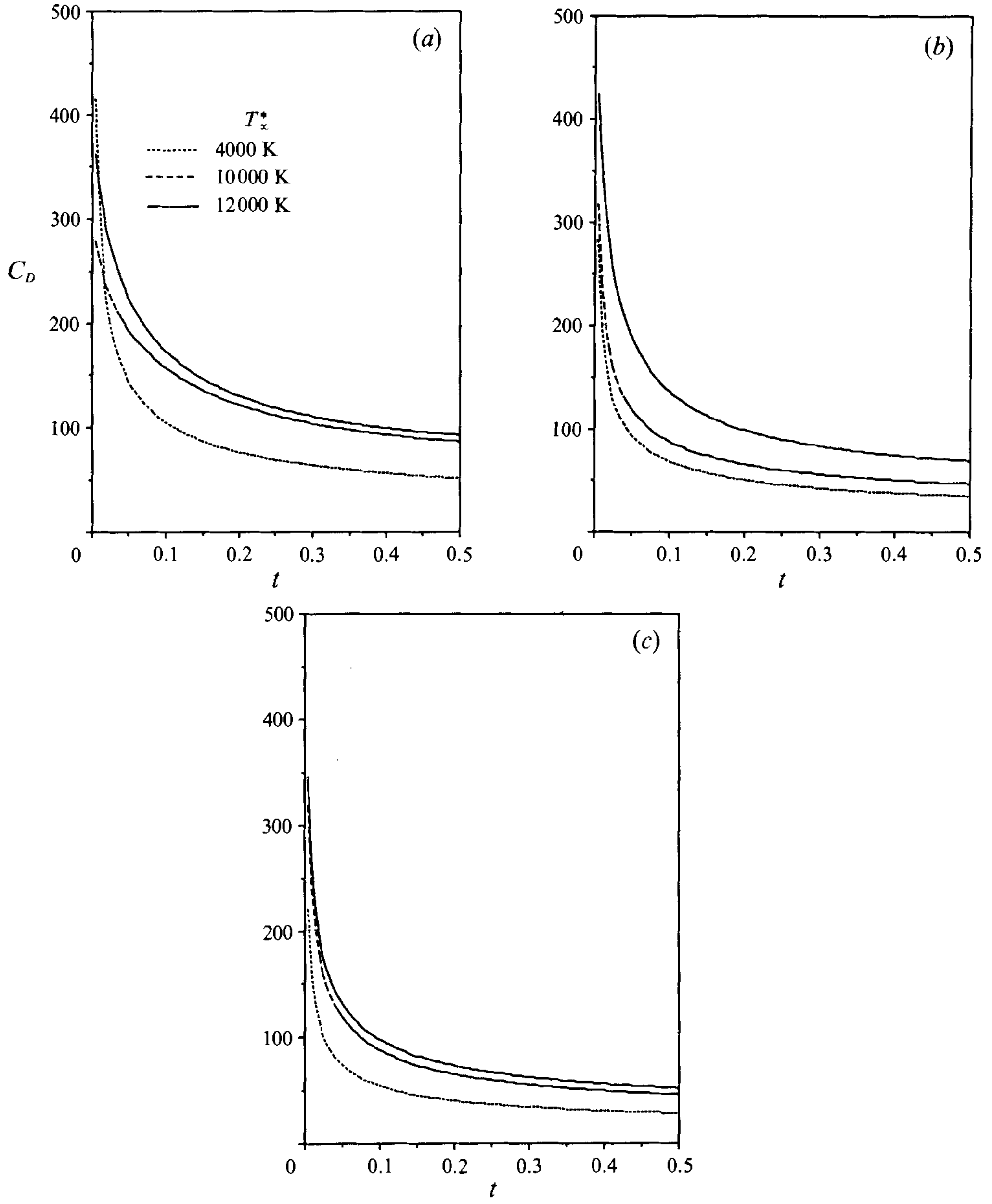

FIGURE 7. Transient total drag coefficient for an Al_2O_3 particle for different plasma free-stream temperatures with (*a*) $T_w^* = 1000$ K, (*b*) = 2000 K, (*c*) = 3000 K.

particle radius 20 μm in the simulation. For a fixed initial particle temperature, the Nusselt number decreases as the free-stream temperature increases. This trend is due to the definition of Nusselt number used in this study. In the case for changing surface temperature, the Nusselt number is defined as

$$Nu = \frac{2Rq^*}{S_\infty^* - S_I^*}, \tag{43}$$

where S_I is the thermal conductivity potential based on the initial sphere temperature.

Thus for the high free-stream temperature, the denominator of (43) is larger than for that of low free-stream temperature while the increase of thermal conductivity due to the increase of particle surface temperature is not large.

For isothermal flow past a solid sphere, the drag coefficient is a function of Reynolds number only. But under a thermal plasma environment, the drag coefficient is a function of the plasma free-stream temperature as well as the initial particle temperature. Figure 7 compares the total drag coefficients calculated including the internal heat conduction under the same conditions used for figure 6. For constant surface temperature, the total drag coefficient increases as the plasma free-stream temperature increases. As the particle surface temperature increases, it is expected that the plasma density and viscosity changes would result in changes in the total drag coefficient. However, during the simulated time spans, particle surface temperature changes on the order of 10 K do not affect the plasma thermodynamic and transport properties significantly. Figure 7 shows the same trends as the case with a constant surface temperature. The resulting increase in drag with high free-stream temperatures, for the constant wall temperature case, is expected because at higher free-stream temperatures the radial temperature profile in the vicinity of the sphere becomes steeper, reducing the thickness of the layer of low-viscosity fluid near the surface. The magnitude of the drag coefficient increases as the surface temperature decreases at constant free-stream temperatures. This finding is in contrast to that of Seymour (1971) who states 'the drag ratio at constant free-stream temperature was found to increase with sphere wall temperature as one would expect due to the viscosity in the fluid near the wall'. However, in Seymour's drag calculation, the contribution of the inertia force to the total drag had been neglected and only the viscous force had been considered. Thus the experimentally measured drag in his study was found to be 10–30% higher than the calculated drag. The fluid density changes more drastically than the viscosity with temperature under the temperature ranges considered in this study. Thus, as the surface temperature is lowered, the density of the fluid increases, resulting in higher inertia forces.

Using one-dimensional heat conduction model, Bourdin *et al.* (1983) concluded that the temperature difference between the surface and the centre of the particle can be less than 5% of the maximum temperature differences when the Biot number is less than 0.02. Their findings agree with ours, where the Biot numbers are usually less than 0.01 so that the temperature distribution inside the sphere is quite uniform due to high heat capacity and thermal conductivity. Thus, the commonly used constant particle temperature assumption is valid under the argon thermal plasma conditions studied here.

7. Conclusions

The time-splitting method suggested by Orszag & Kells (1980) is extended to solve the unsteady compressible plasma flow and heat transfer problem. The present method converges reasonably well with properly chosen time steps. The drag coefficients calculated here agree closely with available experimental measurements.

Present results indicate that the thermal relaxation time required for a particle immersed in argon plasma flow to reach steady state is 2 to 3 times higher than that predicted by Konopliv & Sparrow (1972) using a quasi-steady assumption because the momentum boundary layer develops more slowly than the thermal boundary layer. The particle relaxation time inside the argon thermal plasma is found to be very short so that the use of a steady-state correlation for the calculation of transient particle trajectories and heating histories is acceptable. It is also interesting to note that for the low surface temperature case, it takes a longer time for the flow to reach the steady state since steeper temperature and fluid property gradients near the sphere surface hinder the flow in adjusting to the environment.

It is also found that when internal heat conduction is included, which is close to real particle–plasma flow, the Nusselt number increases as the free-stream temperature decreases due to the slow change of thermal conductivity near the particle surface. However, the drag force increases as the plasma free-stream temperature increases.

The calculated steady-state drag coefficients and Nusselt numbers are higher than those of the constant-property calculations due to the large temperature gradients near the sphere surface which induce rapid changes in the transport properties. This trend agrees qualitatively with previous studies (Lewis & Gauvin 1973; Chen & Pfender 1983; Lee *et al.* 1981).

Finally, the problems of particle interaction with an applied electromagnetic field, particle ablation, particle thermophoresis and droplet motion under the thermal plasma condition need to be rigorously studied in the future in order to understand real gas effects of the plasma–particle interactions.

The authors would like to thank Drs M. Stewart and R. Douglas for their valuable comments. This work is performed under the auspices of the US Department of Energy, contract number DE-AC07-76-ID01570, and was supported in part by the INEL Long-Term Research Initiatives Program.

REFERENCES

ASAMALIEV, M. K., ZHEENBAEV, ZH. ZH., LELIOVKIN, V. M., MAKESHEVA, K. K. & UROSOV, R. M. 1991 Influence of nonisothermicity on drag coefficient of a spherical Al particle in a plasma. *Plasma Chem. Plasma Processing* **11**, 269.

BOURDIN, E., FAUCHAIS, P. & BOULOS, M. 1983 Transient heat conduction under plasma conditions. *Intl J. Heat Mass Transfer* **26**, 567.

CHEN, X. 1986 On the applicability of available expressions for heat transfer to a particle exposed to a thermal plasma flow. *Proc. Intl Conf. on Plasma Science and Technology, Beijing, June 1986*, p. 106. Beijing: Science Press.

CHEN, X. 1988 Particle heating in a thermal plasma. *Pure Appl. Chem.* **60**, 651.

CHEN, X. & PFENDER, E. 1983 Behavior of small particles in a thermal plasma flow. *Plasma Chem. Plasma Processing* **3**, 351.

CHEN, X., QIU, J.-Y. & YANG, J. 1991 An experimental study of the drag force on a sphere exposed to an argon thermal plasma flow. *Plasma Chem. Plasma Processing* **11**, 151.

DENNIS, S. C. R. & WALKER, J. D. A. 1971 Calculation of the steady flow past a sphere at low and moderate flow past a sphere at low and moderate Reynolds numbers. *J. Fluid Mech.* **48**, 771.

DENNIS, S. C. R., WALKER, J. D. A. & HUDSON, J. D. 1973 Heat transfer from a sphere at low Reynolds numbers. *J. Fluid Mech.* **60**, 273.

HSU, K. C. 1982 A self-consistent model for the high intensity free burning argon arc. PhD thesis, University of Minnesota.

KARNIADAKIS,G. E., ISRAELI, M. & ORSZAG, S. A. 1991 High-order splitting methods for the incompressible Navier–Stokes equations. *J. Comput. Phys.* **97**, 414.

KONOPLIV, N. & SPARROW, E. M. 1972 Unsteady heat transfer and temperature for Stokesian flow about a sphere. *Trans. ASME* C: *J. Heat Transfer*, p. 266.

LEE, Y. C., HSU, K. C. & PFENDER, E. 1981 Modeling of particles injected into a d.c. plasma jet. *Fifth Intl Symp. on Plasma Chemistry*, vol. 2, p. 795. Heriot-Watt University, Edinburgh.

LEWIS, J. A. 1971 The motion of particles entrained in a plasma jet. PhD thesis, McGill University.

LEWIS, J. A. & GAUVIN, W. H. 1973 Motion of particles entrained in a plasma jet. *AIChE J.* **19**, 982.

MILLER, R. C. & AYEN, R. J. 1969 Temperature profiles and energy balance for an inductively coupled plasma torch. *J. Appl. Phys.* **40**, 5260.

NGUYEN, H. D., PAIK, S. & CHUNG, J. N. 1991 Application of vorticity integral conditioning to Chebyshev pseudospectral formulation for the Navier–Stokes equation. *J. Comput. Phys.* (in press).

ORSZAG, S. A. & KELLS, L. C. 1980 Transition to turbulence in plane Poiseuille and plane Couette flow. *J. Fluid Mech.* **96**, 159–205.

ORSZAG, S. A., ISRAELI, L. C. & DEVILLE, M. O. 1986 Boundary conditions for incompressible flows. *J. Sci. Comput.* **1**, 75.

PAIK, S., NGUYEN, H. D. & CHUNG, J. N. 1992 A Chebyshev–Legendre spectral method for the solution of flow past a solid sphere: primitive variable formulation. *J. Comput. Phys.* (submitted).

PFENDER, E. 1989 Particle behavior in thermal plasmas. *Plasma Chem. Plasma Processing* **9**, 167S.

ROTTENBERG, M., BIVINS, R., METROPOLIS, N. & WOOTEN, J. K. 1959 *The 3-J and 6-J Symbols.* MIT Press.

SAYEGH, N. N. & GAUVIN, W. H. 1979 Numerical analysis of variable property heat transfer to a single sphere in high temperature surroundings. *AIChE J.* **25**, 522.

SEYMOUR, E. V. 1971 The hydrodynamic drag on a small sphere in an ionized gas. *Trans. ASME* E: *J. Appl. Mech.*, p. 739.

TEMAM, R. 1991 Remark on the pressure boundary condition for the projection method. *Theoret. Comput. Fluid Dyn.* **3**, 181–184.

VARDELLE, A., VARDELLE, M. & FAUCHAIS, P. 1982 Influence of velocity and surface temperature of alumina particles on the properties of plasma sprayed coatings. *Plasma Chem. Plasma Processing* **2**, 255.

WHITE, F. M. 1974 *Viscous Fluid Flow.* McGraw-Hill.